Journal of Sound and Vibration (2000) **238**(5), 757–779
doi:10.1006/jsvi.1999.3108, available online at http://www.idealibrary.com on IDEAL®

DYNAMIC RESPONSE OF AN UNBALANCED ROTOR SUPPORTED ON BALL BEARINGS

M. Tiwari and K. Gupta

Mechanical Engineering Department, Indian Institute of Technology, Delhi, New Delhi-110016, *India*

AND

O. Prakash

Industrial Tribology Machine Dynamics and Maintenance Engineering Center, Indian Institute of Technology, Delhi, New Delhi-110016, *India*

(*Received* 10 *February* 1999, *and in final form* 6 *July* 1999)

The non-linear dynamic analysis of a horizontal rigid rotor having unbalance and supported on ball bearings has been done. The non-linearity is both due to Hertzian contact and the radial internal clearance. The system is excited by the varying compliance frequency and the rotational frequency. For finding out the fixed point and stability of the system the concept of higher order Poincare map and interpolation technique has been applied. The results show the appearance of instability and chaos in the dynamic response as the speed of the rotor-bearing system is changed. Period doubling and mechanism of intermittency have been observed as the routes to chaos. The experimental investigations for a horizontal rotor-bearing system have shown the effect of varying compliance and increase in non-linearity due to radial internal clearance of the ball bearing. The orbit plots, cascade plots and frequency plots bring out the effect of radial internal clearance on the rotor response.

1. INTRODUCTION

Unbalance force in a rotor is an unavoidable effect. Howsoever good the balancing may be for a rotor the unbalance force cannot be completely eliminated. For a horizontal Jeffcott rotor supported on ball bearings the exciting frequencies are because of the unbalance force and the varying compliance effect. The combined effect of unbalance and varying compliance has not been considered by Fukata [1], Mevel and Guyader [2] and Sankaravelu [3]; in these works only the varying compliance effect is considered. The inclusion of the unbalance force makes the system biperiodically excited. The studies undertaken by Day [4], Kim and Noah [5, 6] have considered the effect of unbalance force only, but not varying compliance effect. Also, in references [4–6] the bearing is considered to have only clearance non-linearity. In the present analysis, all the three effects, i.e., the unbalance, the varying compliance and the clearance are studied in addition to non-linearity due to Hertzian contact.

The theoretical results show the appearance of instability and chaos through a route of period doubling and intermittency. The experimental results show the effect of radial clearance on the dynamic response of the ball bearing. The non-linearity of the ball-bearing support results in the appearance of subharmonics and sum and difference combination of rotational and varying compliance frequencies.

0022-460X/00/500757 + 23 $35.00/0

2. PROBLEM FORMULATION

The rotor-bearing system under study has the outer race of the ball bearing fixed to a rigid support and the inner race fixed rigidly to the shaft. A constant vertical radial force acts on the bearing. The excitation is because of the unbalance force which introduces the rotational frequency and the varying compliance vibrations of the bearing which arise because of the geometric and elastic characteristics of the bearing assembly varying according to the cage position [1].

The ball-bearing model considered here has equi-spaced balls rolling on the surfaces of the inner and outer races. There is perfect rolling of balls on the races so that the two points of the ball (A and B) touching the outer and inner races have different linear velocities (Figure 1). The center of the ball has a resultant translational velocity. Therefore,

$$\omega_{cage} = \omega_{ROTOR}\left(\frac{R_i}{R_i + R_O}\right). \tag{1}$$

The varying compliance frequency is given by

$$\omega_{vc} = \omega_{ROTOR} \times BN, \tag{2}$$

where

$$BN = \frac{R_i}{R_i + R_0} \times N_b. \tag{3}$$

The number BN depends on the dimensions of the bearing, for SKF6002, $BN = 3{\cdot}6$.

The damping is estimated by the relation provided by Krämer [7]. The bearing is assumed to be free of local and distributed defects. The ball-race contact deformation of the ball generates a restoring force with non-linear characteristics because of the Hertzian contact. Taking the x and y displacements of the center of the inner race (Figure 1),

$$F_{\theta_i} = C_b(x\cos\theta_i + y\sin\theta_i - \gamma_0)^{1\cdot5}. \tag{4}$$

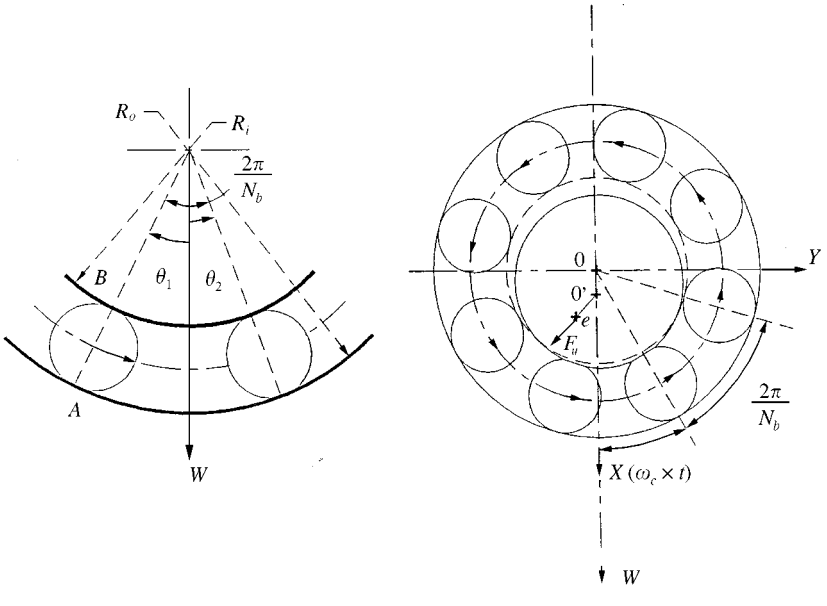

Figure 1. Ball bearing.

The inner race is supported by the rolling balls over an angular contact zone the size of which depends on the size of the radial internal clearance (γ_0) [8]. The values of C_b and n are arrived at by performing the elastic analysis of the Hertzian contact with the inner and outer races and the ball [8], for SKF6002, $C_b = 7{\cdot}055 \times 10^9$ N/m$^{3/2}$. If the expression inside the brackets is greater than zero, then the ball at angular location θ_i is within the angular contact zone and it is loaded giving rise to a restoring force F_{θ_i}. If the expression within the brackets is negative or zero, then the ball is not in the load zone, and the restoring force F_{θ_i} is set to zero. The " + " sign as a subscript in equation (4) signifies this step change in the restoring force expression and models the clearance non-linearity. The total restoring force is the sum of restoring force from each of the rolling elements. Thus, the total restoring force components in the X and Y directions are

$$F_x = C_b \sum (x \cos\theta_i + y \sin\theta_i - \gamma_0)_+^{1{\cdot}5} \cos\theta_i,$$
$$F_y = C_b \sum (x \cos\theta_i + y \sin\theta_i - \gamma_0)_+^{1{\cdot}5} \sin\theta_i. \tag{5}$$

As the shaft rotates, the angle θ_i changes with time (Figure 1) and is given by

$$\theta_i = \frac{2\pi}{N_b}(i-1) + \omega_{cage} \times t, \quad i = 1, \ldots, N_b. \tag{6}$$

Here the reference is the vertical axis which is the direction of the constant vertical force. We see that the angle θ_i is a function of time and this imparts the parametric effect to the system. The system equations are

$$m\ddot{x} + C\dot{x} + C_b \sum_{i=1}^{N_b} (x \cos\theta_i + y \sin\theta_i - \gamma_0)_+^{1{\cdot}5} \cos\theta_i = W + F_u \cos(\omega t),$$
$$m\ddot{y} + C\dot{y} + C_b \sum_{i=1}^{N_b} (x \cos\theta_i + y \sin\theta_i - \gamma_0)_+^{1{\cdot}5} \sin\theta_i = F_u \sin(\omega t), \tag{7}$$

where m is the mass of the rotor supported by bearing and mass of inner race, F_u is the unbalance force and ω is the rotational speed. The system equations (7) are two coupled, non-linear ordinary second order differential equations having parametric effect in them. The stiffness because of its step change behavior, the parametric effect with 1·5 non-linearity and the summation term is non-analytic in nature.

2.1. BI-PERIODICALLY EXCITED SYSTEM

The numerical relationship between the rotational speed and the varying compliance frequency is given by the number BN, equations (2) and (3). It follows from this relationship that the two frequencies are related to each other by the bearing dimensions and the number of rolling elements or balls, which determine the system frequency. Depending on the ratio $(R_i \times N_b)/(R_i + R_0)$, the system time period is large or small. For the bearing JIS6306 taken by Fukata [1], the bearing dimensions and value of BN is given in Table 1.

For SKF6002 $T_{Rotational} = T_{VC} \times \frac{18}{5}$. A long time period makes most of the techniques such as the non-autonomous shooting method [9] computationally inefficient as the variational equation would have to be integrated at each step of the Newton–Raphson algorithm over a long time period. To overcome this problem the method used by Choi and

TABLE 1

Bearing number (*BN*)

Bearing	R_1 (mm)	R_0 (mm)	N_b	*BN*
JIS6306	40·1	63·9	8	3·08
SKF6002	9·37	14·13	9	3·6

Noah [10] for determining the fixed point of a bi-periodic system with incommensurate excitation frequencies is adopted.

If the solution of the system is $\phi(\omega_{VC}t, \omega_{Rotational}t)$, the flow will be intersecting the $(n-1)$th hypersurface at the fixed points

$$x_k^*(0, \omega_{Rotational}t_k) \quad \text{or} \quad x_k^*\left(0, \frac{2\pi t_k}{T_{Rotational}}\right), \tag{8}$$

where $t_k = kT_{VC} = k2\pi/\omega_{VC}$, $k = 0, 1, 2, \ldots$.

Define a parameter τ_k as

$$\tau_k = \begin{cases} \bar{t}_k + 1 & \text{if } 0 \leqslant \bar{t}_k < \frac{1}{2} \\ \bar{t}_k & \text{if } \frac{1}{2} \leqslant \bar{t}_k \leqslant 1, \end{cases} \tag{9}$$

where $\bar{t}_k = (t_k/T_{Rotational}) (\text{mod } 1)$. Since $\bar{t}_k$ is a modulo 1 function its value is always in the range of 0–1. Then the fixed point in the second order Poincare map $P_2(0)$ becomes ϕ_k with τ_k as 1:

$$P_2(0) = \phi_k(0, 1). \tag{10}$$

For a large time period, value of k is large and τ_k is 1. An interpolating technique is utilized with smaller values of k to reduce computation time. By choosing a positive ε less than one, the orbit of second order Poincare map will be composed of those points x_k^* where k satisfies

$$|\tau_k| \leqslant \varepsilon. \tag{11}$$

Therefore, $\{\tau_k\}$ becomes a set of points where τ_k satisfies the condition given by equation (11). Apparently, as ε goes to zero, τ_k tends to 1 [10]. Using this property, the fixed point of the system can be estimated by interpolating each co-ordinate (four state-space variables and 16 elements of the Jacobian for the particular value of k, which defines the time for numerical integration of the extended system [9]) corresponding to $\tau_k = 1$. These values are used in the Newton–Raphson technique.

2.2. METHODS OF SOLUTION AND ANALYSIS

The system equations (7) have been found to have numerical stiffness [9]. For this, the numerical integration technique is of the implicit type based on the backward differentiation algorithm. The subroutine for the backward differentiation technique is obtained from the NAG library. The steady solution is obtained by the non-autonomous shooting method, which also gives the monodromy matrix and nature of bifurcations. The higher order Poincare map is generated for studying the nature of solutions.

3. RESULTS OF THEORETICAL SIMULATION

A ball bearing supporting a rigid horizontal rotor with an unbalance force is taken for theoretical simulation.

3.1. FUKATA'S BEARING

Fukata's [1] bearing (JIS 6306) is considered. The unbalance excitation is taken as 15% of W (58.8 N). The *BN* number for JIS6306 is 3·08 (Table 1), which makes the ratio of the two frequencies a rational number. If the digits in the ratio of the two frequencies do not recur within 16 places after decimal place for double precision, it is as good as irrational number, resulting in quasi-periodic solutions.

At a period of 4200 r.p.m., the frequency spectrum (Figure 2(a)) shows the presence of both, the rotational speed (70 Hz) and the varying compliance frequency (215·6 Hz). Both these frequencies interact to produce sum and difference combination frequencies. From the Poincare map (Figure 2(b)) we see discrete number of points which are due to the ratio being a rational number. At 4800 r.p.m. there is period doubling. In the frequency spectrum (Figure 2(c)) the rotational speed (80 Hz) and half the rotational speed (40 Hz), and the varying compliance frequency (246·4 Hz) appear. From Figure 2(d) we see the closed curve made of discrete points which points to the rational number of the ratio between the two frequencies. At 5400 r.p.m. the frequency spectrum (Figure 2(e)) has a band structure and the Poincare map in Figure 2(f) has a characteristic layered structure pointing to the chaotic nature of the response. For 5400 r.p.m. one Lyapunov exponent is positive.

3.2. RESULTS OF THEORETICAL SIMULATION WITH SKF6002

Three levels of unbalance force have been chosen for parametric study. To simplify the study, a constant unbalance force in the entire speed range is assumed. Two values of radial internal clearance have been considered, 20 and 3 μm.

$\gamma_0 = 20\ \mu$m, $C = 200\ Ns/m$, $F_u = 45\%\ of\ W$: From the response plot (Figure 3) the high-amplitude region starting from 3000 r.p.m. has stable periodic response; in this region the frequency spectra show spikes at multiples of $1X/5$ ($VC = 18 \times 1X/5$). This periodicity at $1T$ continues up to 9000 r.p.m. when period doubling bifurcations take place which shows up as a $1X/10$ component and its multiples visible in the frequency spectra at 9500 r.p.m. (Figure 4). The varying compliance frequency is very weak for this high unbalance level. At around 10 000 r.p.m., periodic $1T$ solution returns but soon changes to $2T$ and from 11 500 r.p.m. chaos appears (Figure 4). The band structure in the frequency spectra (Figure 4) points to a chaotic solution. The chaotic response continues up to 13 000 r.p.m. when it regains periodicity by going into period doubling solutions (Figure 4). At 14 000 r.p.m. and more the periodicity again appears with period $1T$.

The frequency spectra and time response plot (Figure 5) at 17 000 r.p.m. show very strong indications of intermittency as a route to chaos. From Figure 5 it is observed that there seem to be two kinds of waveforms present, i.e., the periodic waveforms AA′ and non-periodic waveform BB′. The intermittent periodic behavior with chaotic behavior represents the competition between two attractors [10]. One attractor is of a periodic nature and the other is a strange attractor.

The analysis for the present case revealed that the bifurcation at 16 200 r.p.m. seems to explode into this intermittent behavior. As the speed is increased, the proportion of periodic wave form decreases as compared to the chaotic waveform. This can be seen in Figure 6 where at 18 000 r.p.m. the periodic waveform (AA′) has considerably reduced.

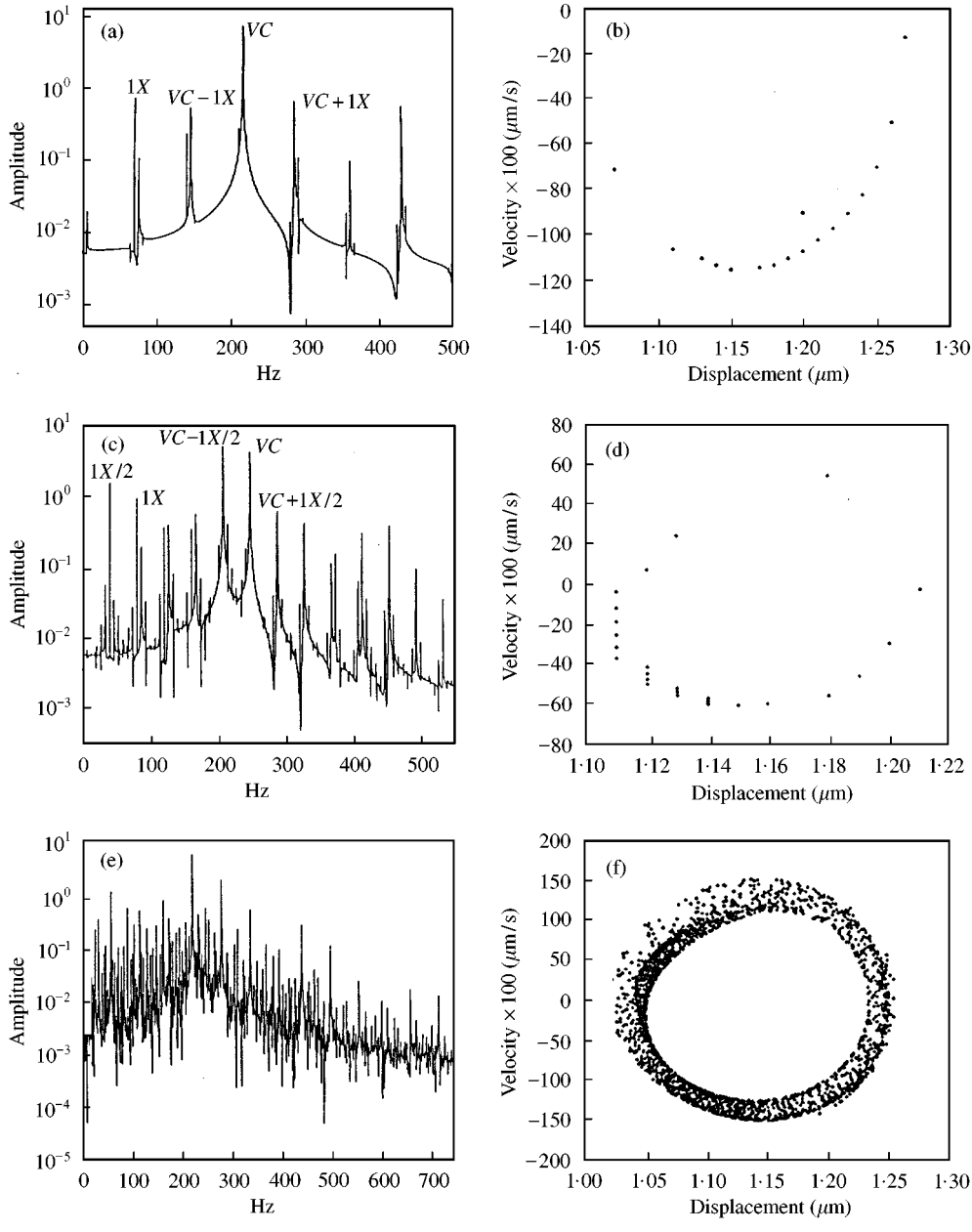

Figure 2. Fukata's bearing.

At 28 700 r.p.m. the time response again explodes into an intermittent character. The eigenvalue of the monodromy matrix indicates loss of stability by going out through $-1{\cdot}0$. Figures 7(a) and 7(b) give the response during two time intervals for the same speed 28 700 r.p.m., 2·1–3 and 3·25–3·6 s respectively. It is obvious that while the response in Figure 7(a) is predominantly periodic, the one in Figure 7(b) is chaotic; this coexistence points to the intermittent behavior. The closed multiloop character of phase plane in Figure 7(a) clearly indicates the presence of periodic response. The phase plane plots in Figure 7(b) indicate the presence of aperiodic response with strong signs of chaos.

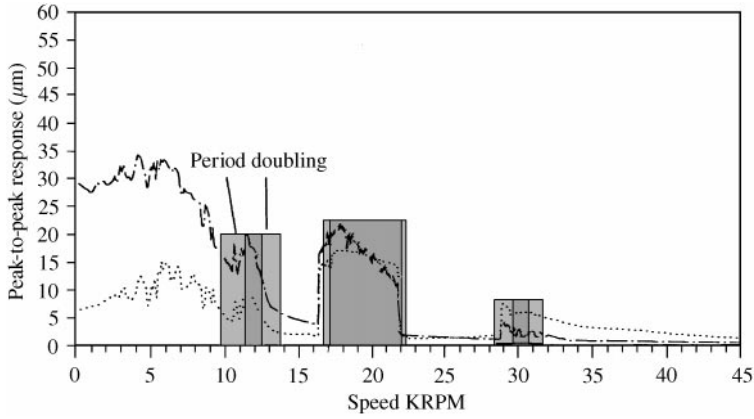

Figure 3. Speed response plot $\gamma_0 = 20\ \mu$m, $C = 200$ Ns/m, $F_u = 0{\cdot}45$ W: ·····, Vertical displacement; —·— horizontal displacement; ▢, unstable one period response; ■, Chaotic response.

$\gamma_0 = 20\ \mu m$, $C = 200$ Ns/m, $F_u = 15\%$ *of* W: The Poincare map at 7000 r.p.m. (Figure 8) shows the characteristic layered structure of a strange attractor, the frequency spectrum and orbit plot also show chaotic response. For this reduced level of unbalance the route to chaos is also seen to be intermittent. At 16 666 r.p.m., the response explodes into intermittent behavior. The eigenvalues of monodromy matrix cross from $+1$ so this becomes an intermittent behavior of type I. In Figure 9, the frequency spectrum shows the band structure and the orbit shows a small dense region surrounded by a less dense structure. From Figure 9 it becomes clear that the intermittent mechanism develops a smaller periodic orbit and another bigger aperiodic orbit. The smaller orbit is because of the periodic smaller amplitude waveform and the bigger aperiodic waveform produces the chaotic response.

$\gamma_0 = 20\ \mu m$, $C = 200\ Ns/m$, $F_u = 5\%$ *of* W: The speed response plot for the present case of reduced unbalance is given in Figure 10. Three regions of chaotic response are identified. The three regions are 3000–6000, 8000–11000 and 16600–22000 r.p.m.

From analysis it is observed that up to about 3000 r.p.m. the response was stable and periodic. The spectra for both the vertical and horizontal displacement were essentially line spectra. At 3000 r.p.m. (Figure 11), the response becomes chaotic. At 5000 r.p.m. the chaotic nature of response is maintained. At 7000 r.p.m. the analysis reached periodic nature of response which at 9000 r.p.m. goes back to chaotic nature (Figure 11) with the $1X/2$ component visible in the frequency spectrum.

From 11 000 to 16 600 r.p.m., the response is low amplitude and periodic. At 16 700 r.p.m. the response suddenly turns chaotic by intermittency as indicated by the time response in Figure 12. The time response waveform shows "bursts" as aperiodic behavior in between low-amplitude periodic waveforms. At 17 000 r.p.m., the aperiodic waveform occupies more time than the periodic waveform (Figure 12). At 22 000 r.p.m. the response returns to periodic behavior as shown in Figure 13.

The reduction of unbalance force makes the VC stronger compared to the $1X$ frequency component as can be seen by comparing the frequency spectra in Figures 4 and 11; also, the extent of chaotic response increases.

$\gamma_0 = 3\ \mu m$, $F_u = 45\%$ *of* $W = 6\ N$, $C = 200\ Ns/m$: There are three regions of high amplitude, Figure 14, in the speed response of a rotor supported on the bearings with the given characteristics. The first region and the third have chaotic nature of response. From

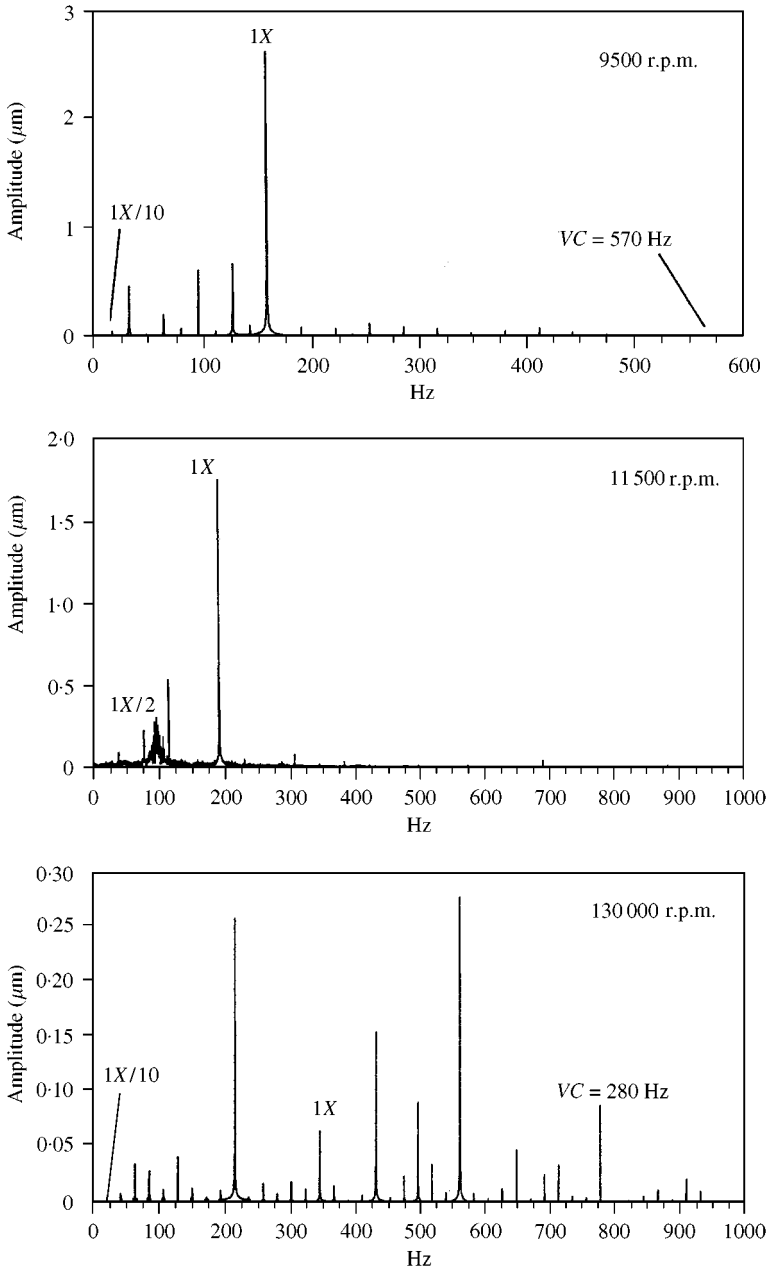

Figure 4. Frequency spectra of horizontal displacement response $\gamma_0 = 12\ \mu$m, $C = 200$ Ns/m, $F_u = 0{\cdot}45$ W.

Figure 15 of the response plots of frequency components $1/2X$, $1X$, $2X$, $3X$, $4X$, $5X$, it can be seen that the peak "A" gradually shifts down in order of the frequency component. This characteristic is also observed in experimental studies.

The region up to 12 000 r.p.m. has periodic solution ($1T$). From 12 240 r.p.m., period doubling takes place and suddenly chaotic response develops from 12 250 r.p.m. onwards. The sudden development of chaotic response from period doubling points to the

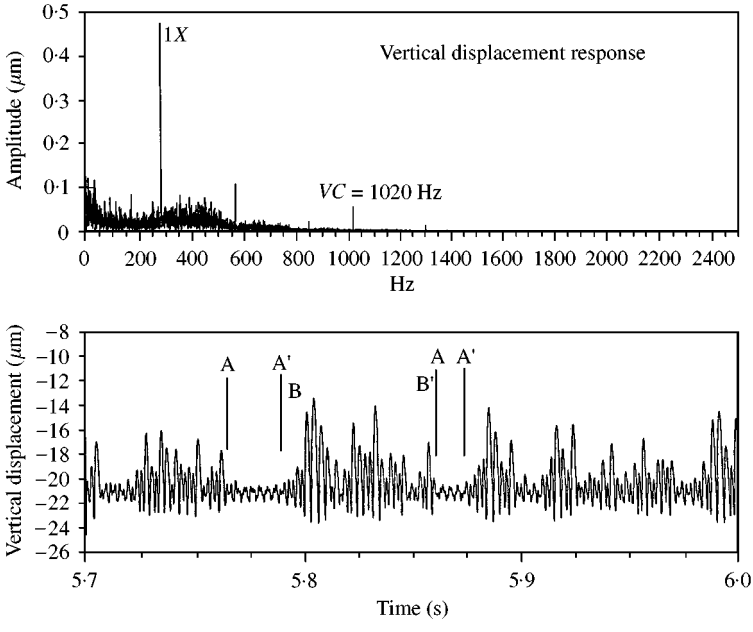

Figure 5. Frequency spectrum and time response plot, $\gamma_0 = 20\ \mu$m, $C = 200$ Ns/m, $F_u = 0{\cdot}45$ W, 17 000 r.p.m.

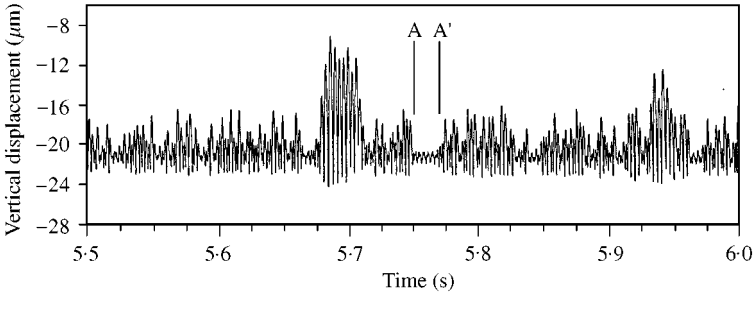

Figure 6. Time response plot, $\gamma_0 = 20\ \mu$m, $C = 200$ Ns/m, $F_u = 0{\cdot}45$ W, 18 000 r.p.m.

intermittency mechanism of type III [11]. The time response plot for 12 250 r.p.m., Figure 16, shows intermittent bursts of non-periodic response.

The chaotic response regains stability at 15 500 r.p.m. The response remains stable up to 27 150 r.p.m. when period doubling takes place (Figure 17). The frequency spectra have clear peaks at $1X/10$. From 27 250 r.p.m. the response becomes chaotic again and at 33 000 r.p.m., the response (Figure 17) becomes period doubled with no sign of chaos. The chaotic orbit which was developing a periodic orbit within it at 32 000 r.p.m. (Figure 17) takes a well-defined periodic form at 33 000 r.p.m. The response retains its period-doubled nature till 37 100 r.p.m.

$\gamma_0 = 3\ \mu m, C = 200\ Ns/m, W = 6\ N, F_u = 15\%\ of\ W$: For a low clearance value of 3 μm and unbalance force lower compared to the last case (45% of W), the system is found to have strong linear characteristics. From the response plot (Figure 18), the regions of high-amplitude AA″ and BB″ are not regions of instability.

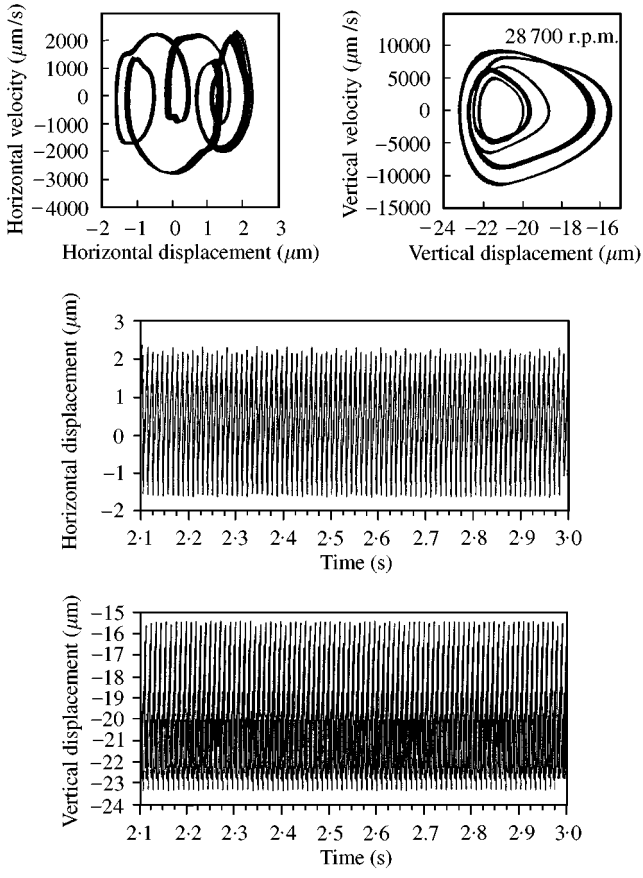

Figure 7(a). Phase plane and time response plots 28 700 r.p.m. from 2·1 to 3·0 s.

The two frequencies $1X$ and VC interact to produce a linear combination ($VC \pm nx$) (Figure 19). It is also seen that the orbit has a "net" structure, resulting because of multifrequency response with a very large time period (Figure 19).

4. EXPERIMENTAL ANALYSIS

Experiments have been conducted to investigate the effect of radial internal clearance and the unbalance force on the dynamic response of a horizontal rotor. The speed range over which the rotor is operated is such that the first critical is not crossed so the experimental analysis is that of a rigid rotor. The signals have been acquired by displacement and acceleration transducers after which the data are processed to give Bode, cascade, orbit, time response and frequency plots. The analysis brings out the appearance of subharmonics and superharmonic frequency components.

4.1. ESTIMATION OF BEARING STIFFNESS

An experimental set-up is used for determining the bearing stiffness [12]. The set-up is designed to be a rigid, horizontal Jeffcott rotor supported on anisotropic bearings. In this

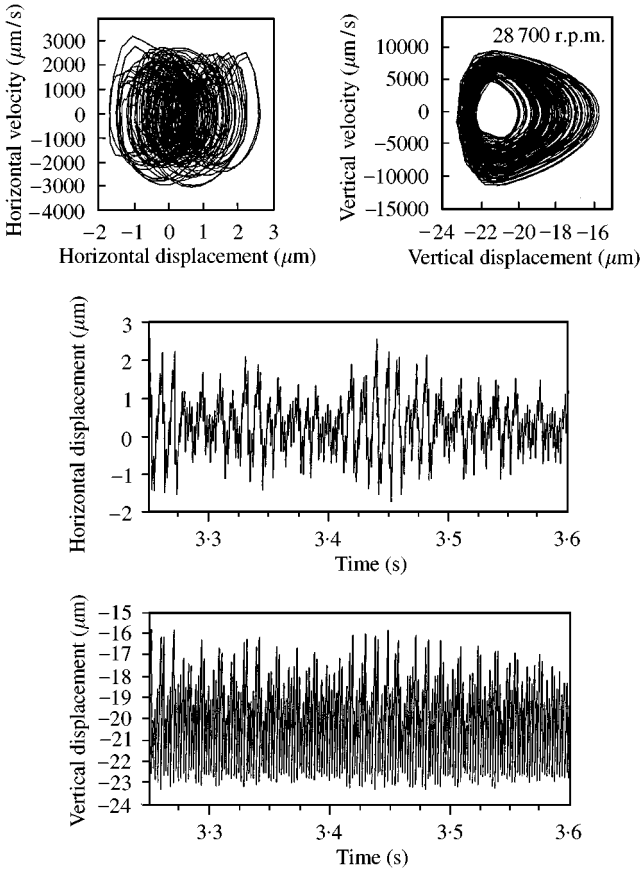

Figure 7(b). Phase plane and time response plots 28 700 r.p.m. from 3·25 to 3·6 s.

case the displacement response in the horizontal and vertical directions would peak at different speeds corresponding to the bearing stiffness in the two directions [7]. The shaft is supported by deep groove ball bearings of known radial internal clearance. The bearing supports are rigid in the vertical and horizontal directions. The shaft stiffness, assuming the ends of the shaft supported by ball bearings as simple supports allowing rotation, is $K_s = 1{\cdot}6 \times 10^8$ N/m. The bearing stiffness as found out theoretically from Gargiulo's [13] and Tamura's [14] methods is of the order of 10^7 N/m so a shaft with stiffness about 10 times that of the bearings can be taken to be rigid.

The shaft is coupled to a motor with a flexible coupling. The motor speed is controlled with a feedback controller which gets the signals from an eddy current probe. The signals are obtained with the help of proximity probes in the horizontal and vertical directions. These two signals are input into a dual-channel spectrum analyzer (DSA; HP 3582A). The rotor system is horizontal and the bearing supports have clearance which introduces anisotropy. There is a very strong $2X$ component and also higher harmonics [$3X$, $4X$, ...] which appear due to clearance and anisotropic effect [15]. It is observed from the DSA that the amplitude of $2X$ and higher harmonics peak at two frequencies. These two frequencies give us an estimate of the two natural frequencies corresponding to the stiffness in the vertical and horizontal directions. The theoretical results also show the appearance of peaks for nX frequency components at $1/n$ times the critical speed.

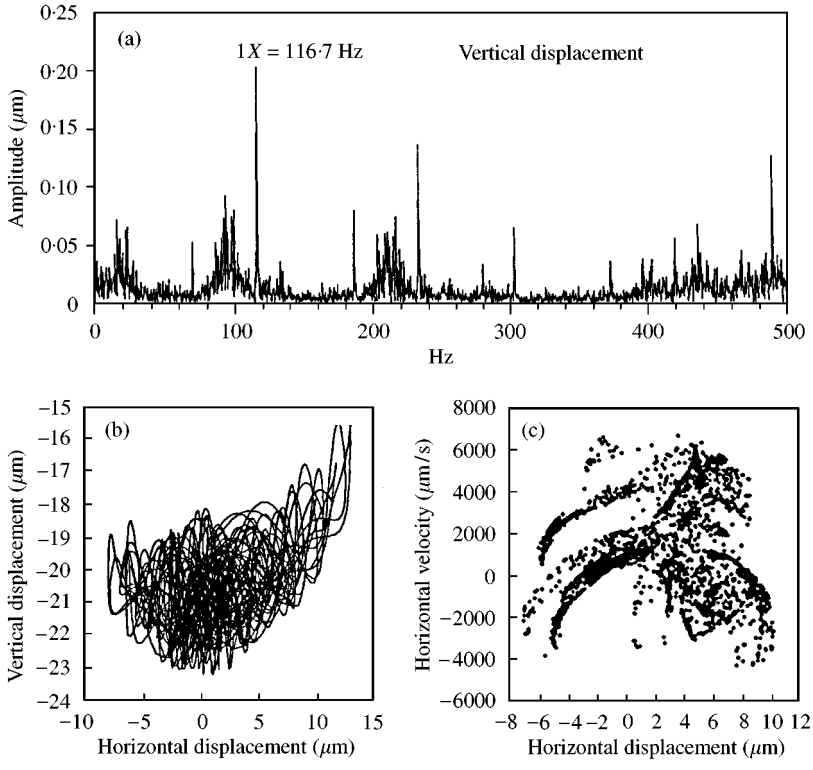

Figure 8. Frequency spectrum, orbit plot and Poincare map, $\gamma_0 = 20$ μm, $C = 200$ Ns/m, $F_u = 0{\cdot}15$ W, 7000 r.p.m.

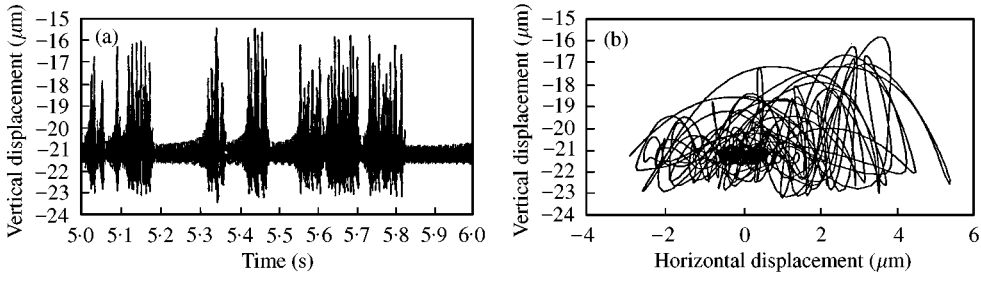

Figure 9. Time response and orbit plot, $\gamma_0 = 20$ μm, $C = 200$ Ns/m, $F_u = 0{\cdot}15$ W, 16 666 r.p.m.

The rotor is run from 0 to 10 000 r.p.m. and the vertical and horizontal displacement responses are fed in the DSA. The $3X$ and $4X$ frequency components are tracked and at various speeds the averaged r.m.s. amplitude for 64 samples is noted. The mass of the shaft and disc exerts a constant force of about 6 N at each bearing support. The level of unbalance is about $2{\cdot}4 \times 10^{-6}$ kg m.

From Figures 20(a) and 20(b) C2-type bearing (radial internal clearance $\gamma_0 \approx 2{\cdot}5$ μm), the amplitudes of $3X$ and $4X$ peak at two frequencies, i.e., 300 and 520 Hz for the vertical direction and 280 and 420 Hz for the horizontal direction. The critical speed is 18 000 r.p.m. (300 Hz) in the horizontal direction and 25 200–31 200 r.p.m. (420–520 Hz) in the vertical direction. From the theoretical results, Figure 18, it can be seen that the critical speeds are

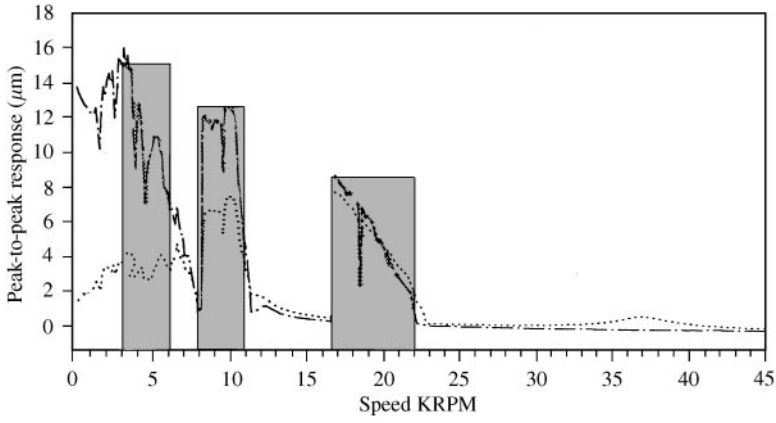

Figure 10. Speed response plot, $\gamma_0 = 20\ \mu$m, $F_u = 0{\cdot}05\ W$, $C = 200$ Ns/m: ·····, Vertical displacement; —·—, horizontal displacement; ■, chaotic response.

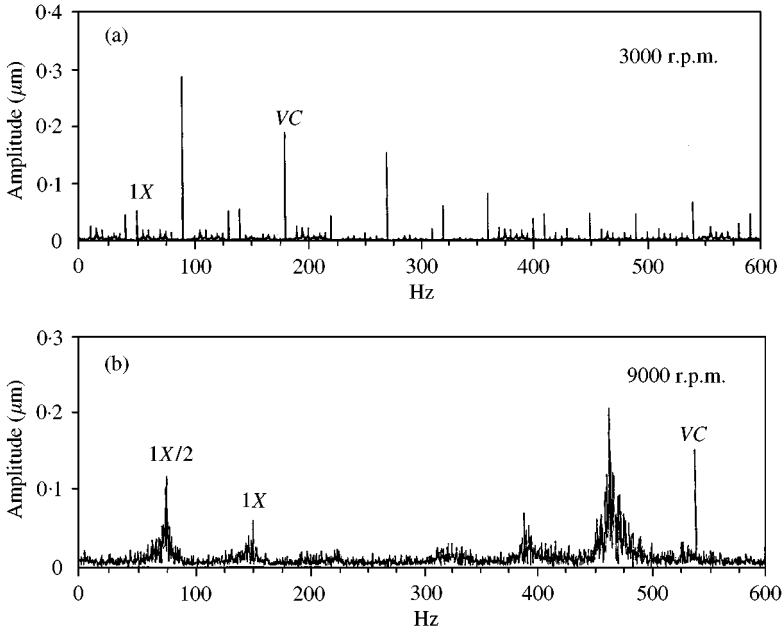

Figure 11. Frequency spectra of vertical displacement response, $\gamma_0 = 20\ \mu$m, $C = 200$ Ns/m, $F_u = 0{\cdot}05$ W.

15 000 and 41 000 r.p.m. The observations made from the theoretical simulation and experimental observations are close. The difference between the experimental and theoretical observations (Figures 15 and 20(a), (b)) is because of the limitations in the experimental set-up of controlling the vertical force at the bearing support at 6 N and in theoretical analysis the unbalance force is a constant force throughout the speed range unlike the experimental condition. The qualitative matching between theory and experiment is good because both observations show the peaking of $3X$ and $4X$ components at $\frac{1}{3}$rd and $\frac{1}{4}$th of the critical speed (on the DSA at the same frequency).

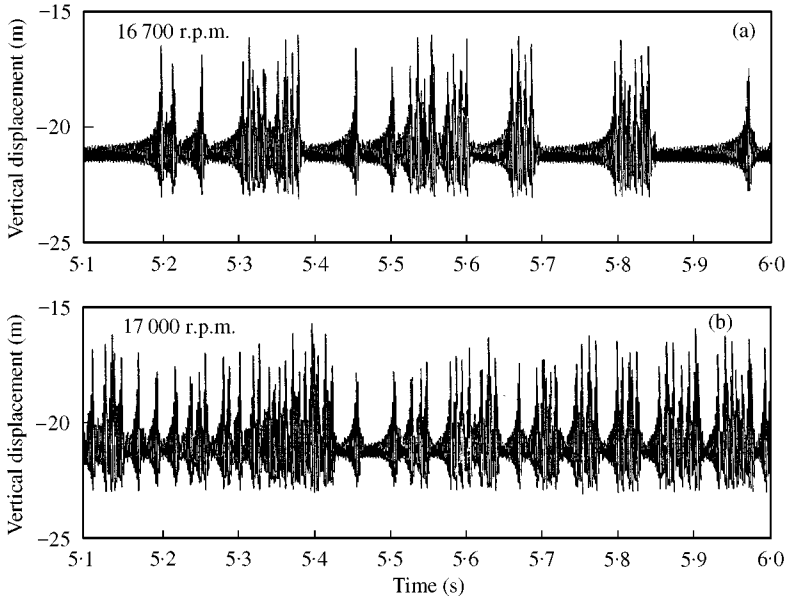

Figure 12. Time response, $\gamma_0 = 20$ μm, $C = 200$ Ns/m, $F_u = 0{\cdot}05$ W.

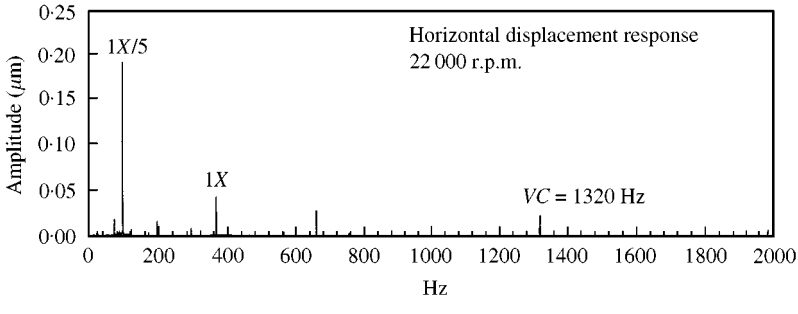

Figure 13. Frequency spectrum, $\gamma_0 = 20$ μm, $C = 200$ Ns/m, $F_u = 0{\cdot}05$ W.

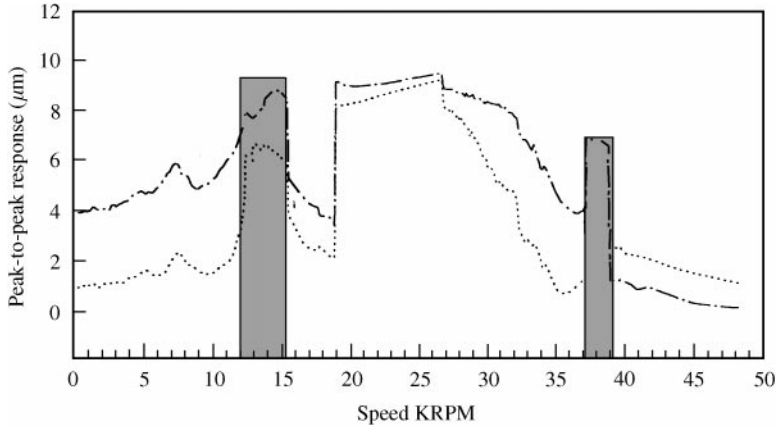

Figure 14. Speed response plot, $\gamma_0 = 3$ μm, $C = 200$ Ns/m, $F_u = 0{\cdot}45$ W: ·····, Vertical displacement; —·—, horizontal displacement ■, chaotic response.

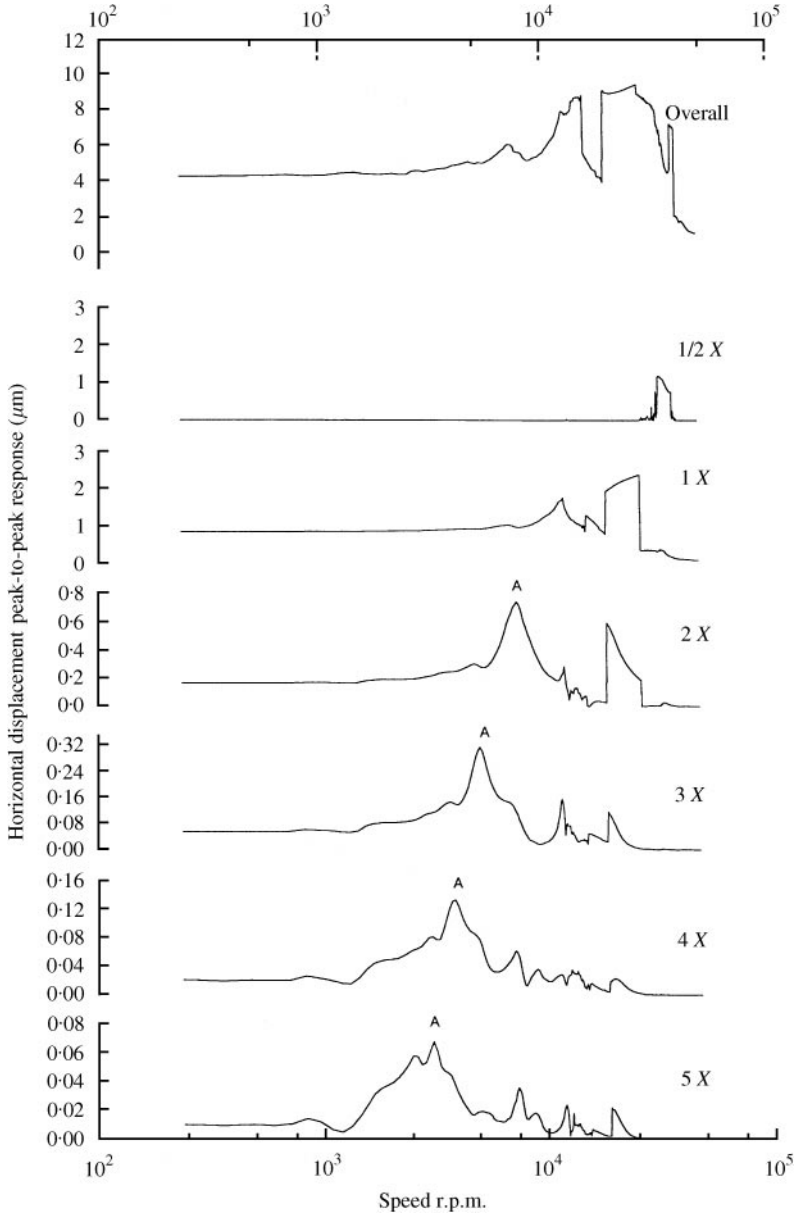

Figure 15. Speed versus response of frequency components.

4.2. ANALYSIS OF RESULTS AND DISCUSSION

For studying the non-linear effect of a ball bearing an experimental set-up (Figure 21) is used. The rotor is supported by bush bearing and the ball bearing. The disk is mounted unsymmetrically as close as possible to the ball bearing support so that the static load coming on the ball bearing is maximum. The static load on the ball bearing is determined experimentally by mounting the bearing support on a load cell and is found to be 6 N. The natural frequency of this rotor-bearing system is estimated theoretically by the transfer

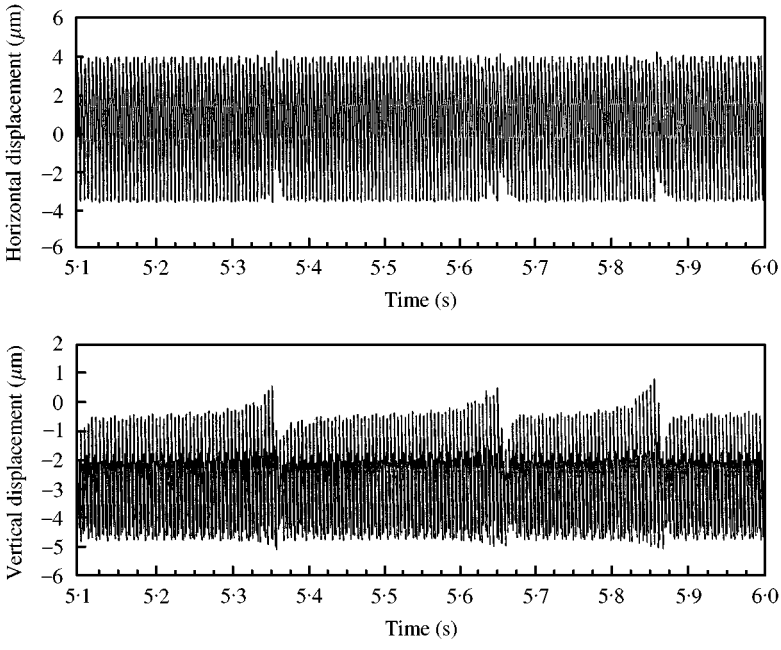

Figure 16. Time response, $\gamma_0 = 20$ μm, $C = 200$ Ns/m, $F_u = 0{\cdot}45$ W, 12 250 r.p.m.

matrix method which matches with those obtained experimentally by rap test. The values obtained are shown in Table 2.

The proximity probes are mounted close to the disk. The horizontal and vertical response signals are fed into a digital vector filter (DVF) which is used for filtering (or band rejecting) $1X$ signal. The output from the DVF is fed into the data-acquisition unit 108 DAUI of Bently Nevada. After the sampling run is completed the data is downloaded on to the PC with the help of ADRE for Windows (Bently Nevada). This software is also used for processing the data to obtain Bode, cascade, and orbit plots.

Two different levels of radial internal clearances are taken up for study SKF 6002-type C2 with radial clearance of about 2·5 μm and SKF 6002-type C5 with radial clearance of 20 μm. The rotor speed is varied up to 10 500 r.p.m.

4.2.1. *Cascade plots*

Two-sided cascade plots have been generated from the acquired signal in which $1X$ is band rejected (Figure 22). The plots show the forward and backward whirl frequency components. The cascade plots are for C2- ($2\gamma_0 = 5$ μm) and C5- ($2\gamma_0 = 40$ μm) type bearings (Figure 22(a) and 22(b) respectively). In the cascade plots $2X$ clearly develops two peaks in the forward vibration component. For the smaller radial internal clearance the strength of $2X$ is weak (Figure 22(a)) compared to the $2X$ component for higher radial internal clearance (Figure 22(b)). Also, the first peak develops weakly for the smaller radial internal clearance. The superharmonics like $3X$ also develop and the strength for higher radial internal clearance is higher. The appearance of $3{\cdot}6X$ shows the varying compliance frequency, as seen theoretically by equation (3). The varying compliance frequency component develops strongly for increased radial internal clearance. The appearance of superharmonics is seen from the theoretical study (Figure 19) and also from other reported

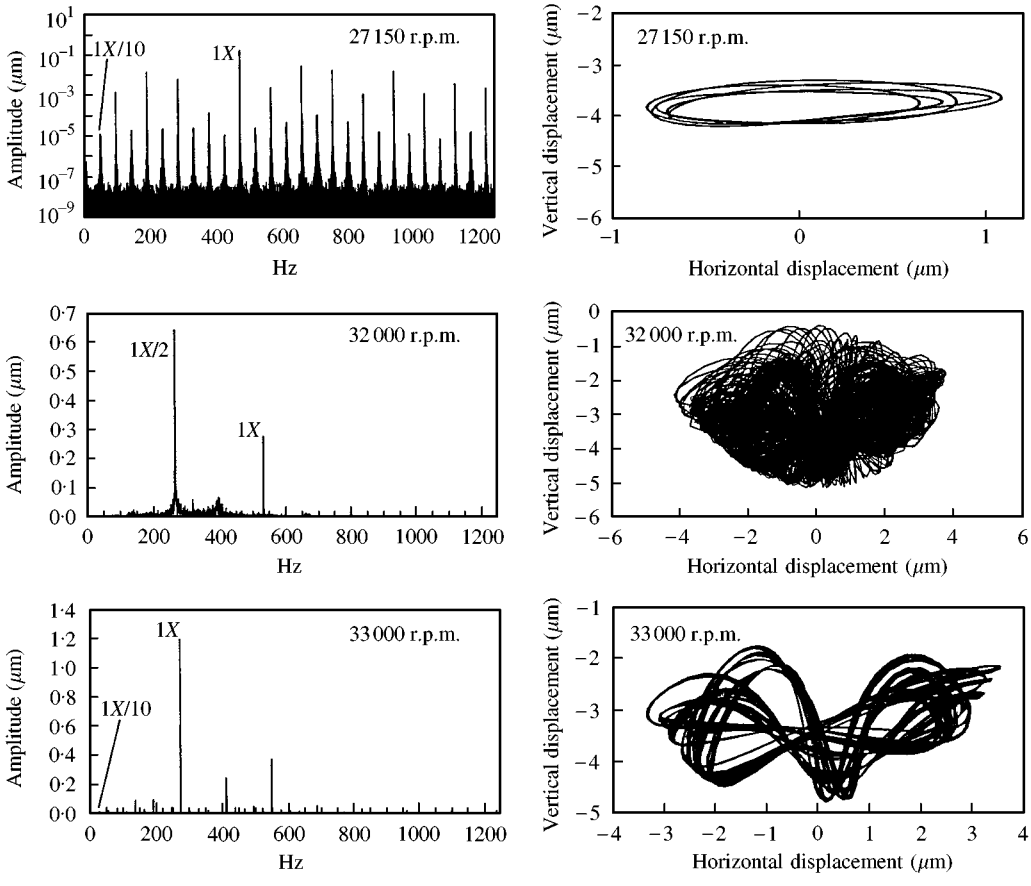

Figure 17. Frequency spectra of horizontal displacement and orbit plots, $\gamma_0 = 3$ μm, $C = 200$ Ns/m, $F_u = 0{\cdot}45$ W.

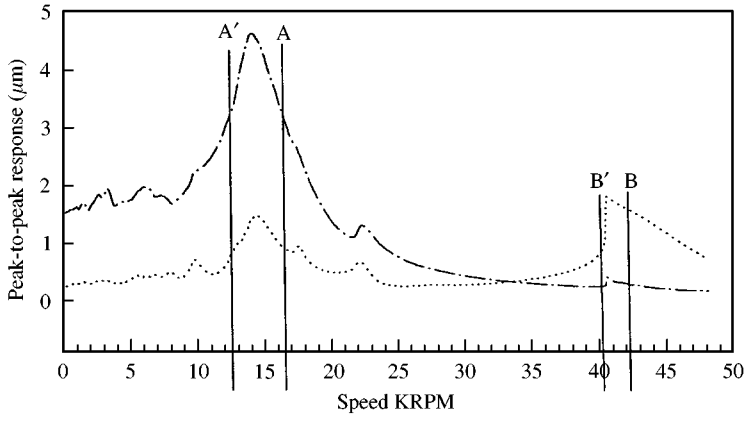

Figure 18. Speed response plot, $\gamma_0 = 3$ μm, $F_u = 0{\cdot}15$ W, $C = 200$ Ns/m: ·····, Vertical displacement; —·—, horizontal displacement.

works studying radial clearance at the rotor support [11]. The experimental reporting of the varying compliance and its dependence on radial internal clearance is done in this study, which has not been reported in any other work.

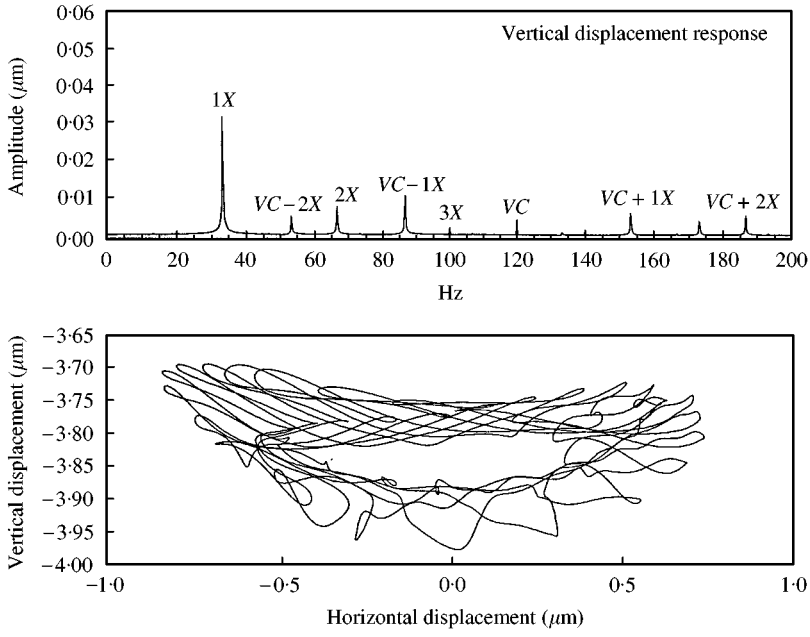

Figure 19. Frequency spectrum and orbit plot, $\gamma_0 = 3$ μm, $C = 200$ Ns/m, $F_u = 0{\cdot}15$ W, 2000 r.p.m.

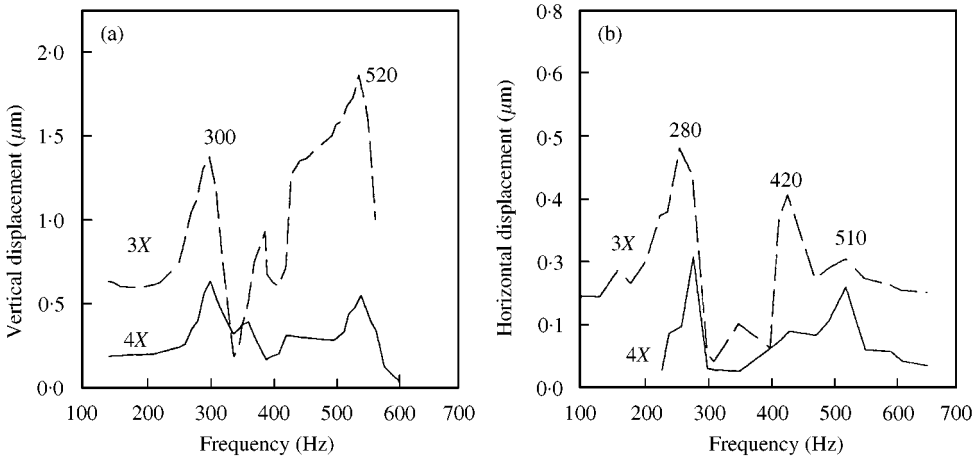

Figure 20. Response plots for $3X$ and $4X$ frequency components.

The reverse vibration components for the lower radial internal clearance are weak as compared to the higher radial internal clearance. This is because of the increased anisotropy at the bearing support due to increased radial internal clearance. The increase in the backward whirl components due to support anisotropy has been shown by Muszynska [16]. From the cascade plots it is seen that for a frequency range of 200–400 Hz and a speed range of 3000–6000 r.p.m. for the forward whirl components the spectra for larger clearance (Figure 22(b)) show larger number of frequency components as compared to the smaller clearance (Figure 22(a)). The spectra (Figure 22(b)) show $4{\cdot}6X$ and $4X$ for the larger radial internal clearance. The increase in radial internal clearance increases non-linearity and the response shows up many subharmonics and superharmonics.

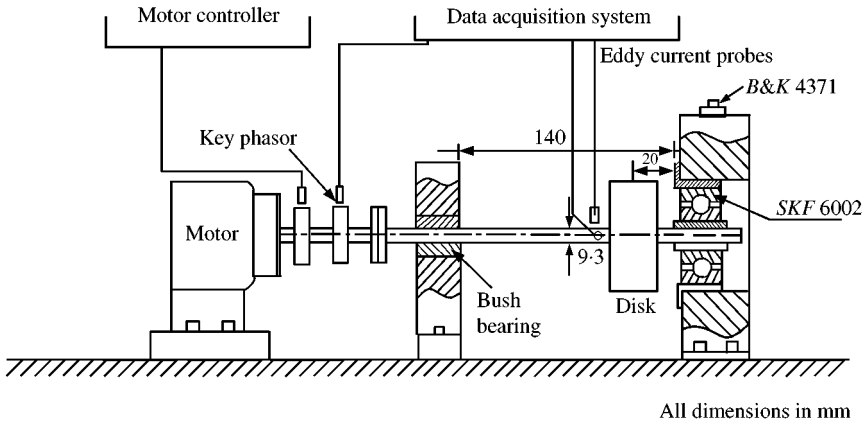

Figure 21. Experimental rig.

TABLE 2

Natural frequencies of the rotor

	Higher frequency (Hz)	Lower frequency (Hz)
Theoretical	369·6	214·4
Experimental	300	200

The result of multifrequency response results in the orbit developing a net structure which has been shown in the theoretical results (Figure 19). The experimental results also show the net structure of the orbit plots (Figure 23). As speed is increased the net structure changes to form a near-elliptical structure at higher speed (above 8500 r.p.m.) because the increased unbalance force makes the $1X$ dominant over the varying compliance and subharmonic frequencies. The frequency spectra (Figures 24(a) and 24(b)) obtained after band rejecting $1X$, for the rotor supported on C2 (lower clearance) and C5 (higher clearance, Figures 24(c) and 24(d)) show the effect of radial internal clearance on the response. The frequency spectra for C5-type bearing at a speed of 5020 r.p.m. ($1X = 83{\cdot}7$ Hz, $VC = 301{\cdot}2$ Hz) show the appearance of $\frac{1}{2}X$, $2X$, $3X$, and $4X$. The linear combinations of the varying compliance frequency and rotational frequency also appear as seen in the theoretical result (Figure 19). For lower radial internal clearance (Figures 24(a) and 24(b)) the $2X$ component is the only well-developed peak. There is almost no sign of well-developed superharmonic and subharmonic components for lower radial internal clearance (Figures 24(a) and 24(b)), which strengthens the argument for decreased non-linearity due to decrease in radial internal clearance.

5. CONCLUSIONS

The theoretical analysis for a rigid horizontal rotor-ball-bearing model with unbalance force shows that multifrequency excitation due to varying compliance and unbalance force results in a response which has regions of instability and chaos. The route to chaos is seen to be intermittency mechanism by period-doubling behavior. Period doubling results in the appearance of $1X/10$ (for SKF6002) and its multiples. Frequency spectra displays multiples of $1X$ and VC and the linear combination of the two frequencies.

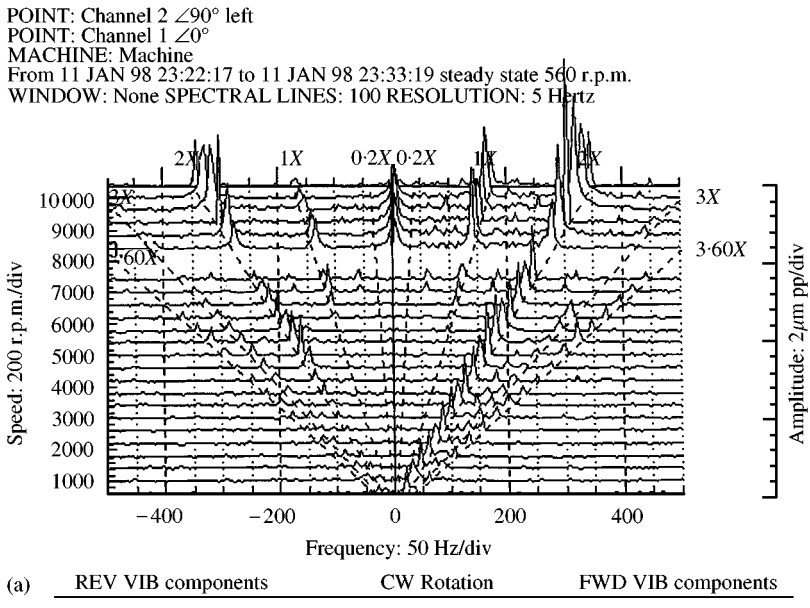

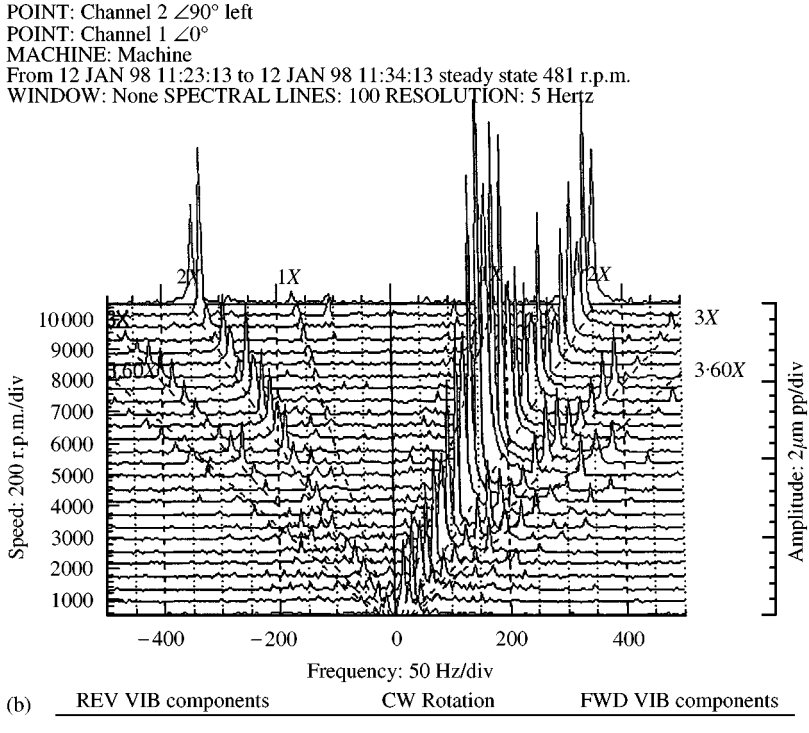

Figure 22. Cascade plot (Full vibration spectrum), 1*X* notched: (a) C2 type (b) C5 type.

The results of experimental analysis match with the theoretical results. The results show that bearing clearance affects the anisotropic nature of the bearing support. The result of increased clearance is to increase the strength of superharmonics, and the strength of backward whirl components. Higher clearance generates more sub-harmonic components

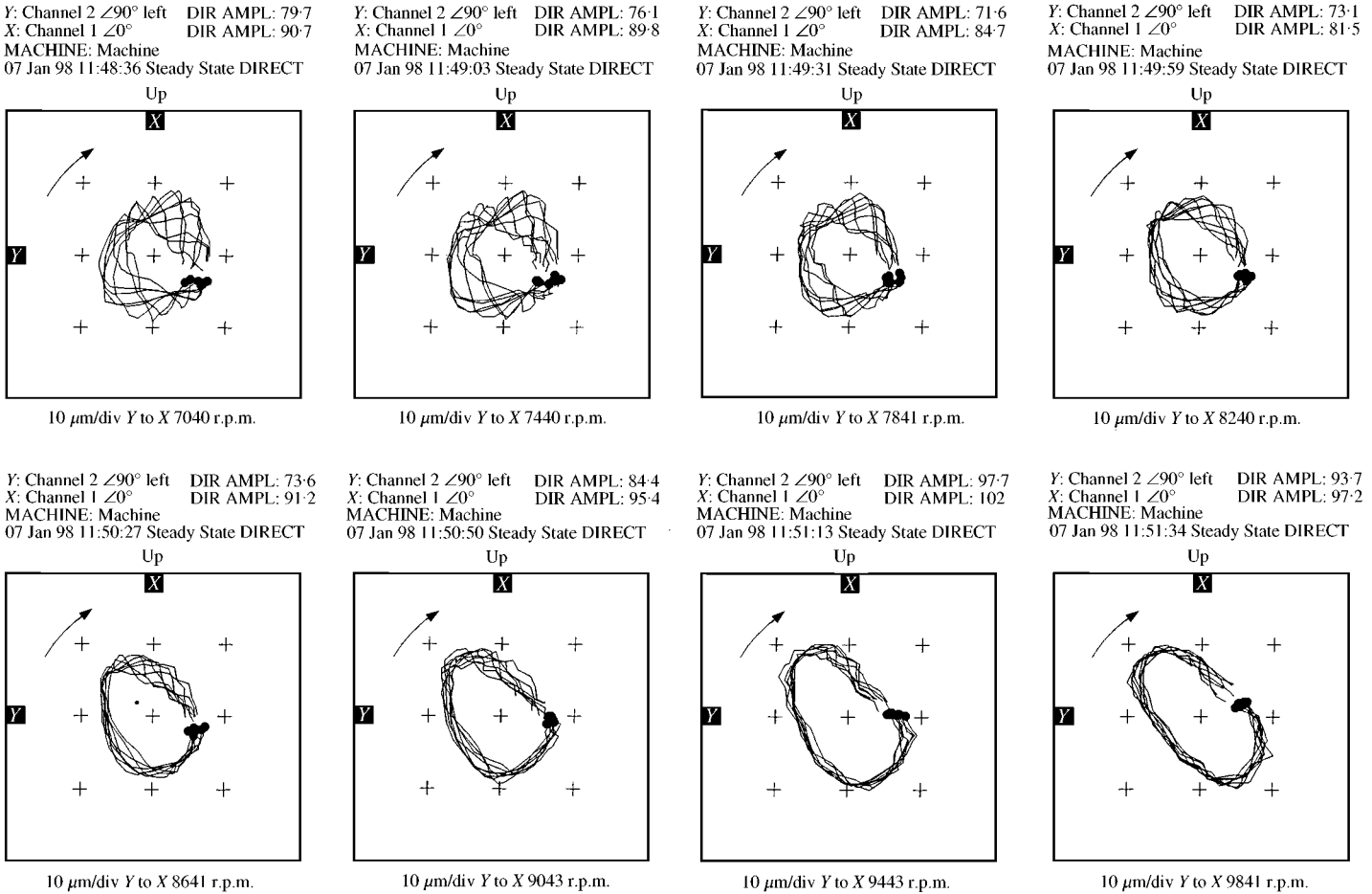

Figure 23. Orbit plots C5 type.

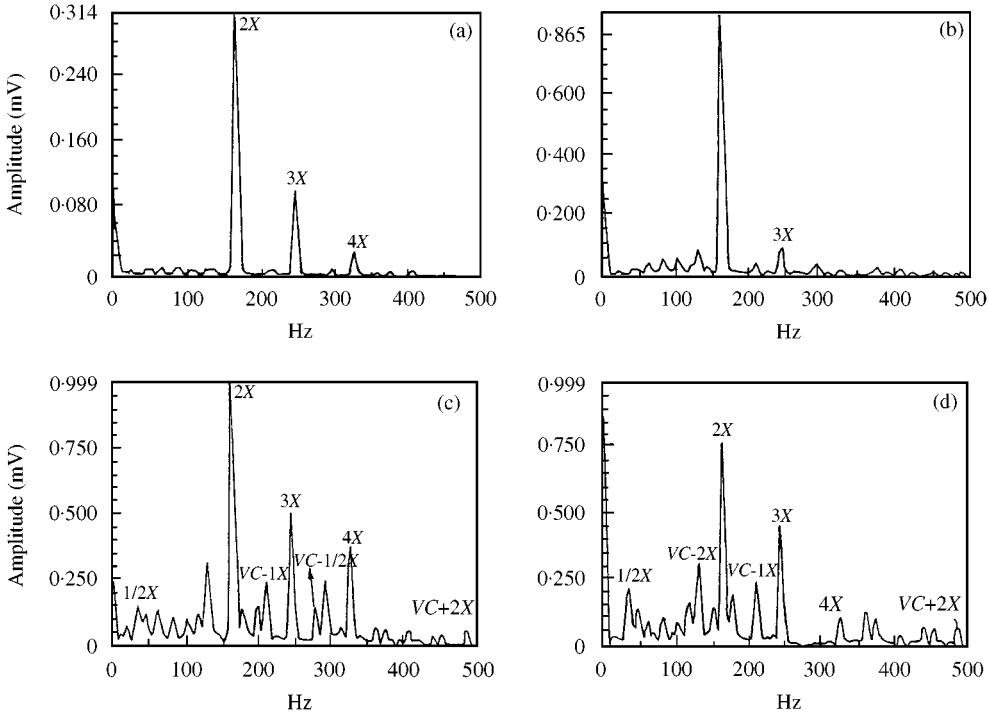

Figure 24. Frequency spectra 5020 r.p.m. low unbalance: (a) vertical displacement *C*2, (b) horizontal displacement *C*2, (c) vertical displacement *C*5 and (d) horizontal displacement *C*5.

in response compared to the case when the bearing has lesser clearance. The orbit plots have a "net" structure which points towards a multifrequency response. The frequency spectra show the appearance of a linear combination of the varying compliance and rotational frequency. The experimental analysis could not show the occurrence of a chaotic phenomenon.

ACKNOWLEDGMENTS

The bearings for the experimental analysis were provided with precise measurement of the relevant dimensions by SKF R&D, France. The help provided by Mr. M. Gorenne, Director R&D SKF, France is gratefully acknowledged.

REFERENCES

1. S. FUKATA, E. H. GAD, T. KONDOU, T. AYABE and H. TAMURA 1985 *Bulletin of the JSME* **28**, 899–904. On the radial vibrations of ball bearings (computer simulation).
2. B. MEVEL and J. L. GUYADER 1993 *Journal of Sound and Vibration* **162**, 471–487. Routes to chaos in ball bearings.
3. A. SANKARAVELU, S. T. NOAH and C. P. BURGER 1994 *Nonlinear and Stochastic Dynamics*, Vol. AMD-192/DE-78, 313–325. ASME. New York: Bifurcation and chaos in ball bearings.
4. W. B. DAY 1987 *Quaterly of Applied Mathematics* **XLIV**, 779–792. Asymptotic expansions in nonlinear rotordynamics.
5. Y. B. KIM and S. T. NOAH 1990 *Nonlinear Dynamics* **1**, 221–241. Bifurcation analysis for a modified jeffcott rotor with bearing clearances.

6. Y. B. KIM and S. T. NOAH 1996 *Journal of Sound and Vibration* **190**, 239–253. Quasi periodic response and stability analysis for a nonlinear jeffcott rotor.
7. E. KRÄMER 1993 *Dynamics of Rotors and Foundations*, 135–141. New York: Springer-Verlag.
8. T. A. HARRIS 1984 *Roller Bearing Analysis*, New York: John Wiley and Sons.
9. M. TIWARI, K. GUPTA and O. PRAKASH 1998 *Proceedings of ISROMAC*-7, 22–26 February, *Hawaii U.S.A.*, Vol. B. 960. Nonlinear dynamic analysis of a rigid rotor supported on a deep groove ball bearing.
10. SANG-KYU CHOI and S. T. NOAH 1992 *Nonlinear Dynamics* **3**, 105–121. Response and stability analysis of piecewise linear oscillations under multi-forcing frequencies.
11. ALI H. NAYFEH and BALAKUMAR BALACHANDRAN 1994 *Applied Nonlinear Dynamics Analytical, Computational, and Experimental Methods*. New York: John Wiley and Sons Inc.
12. M. TIWARI, K. GUPTA and O. PRAKASH 1998 *Journal of Sound and Vibration*. Effect of radial internal clearance of a ball bearing on the dynamics of a balanced, horizontal rotor (accepted for publication).
13. E. P. GARGIULO JR. 1980 *Machine Design* 107–110. A simple way to estimate bearing stiffness.
14. H. TAMURA and Y. TSUDA 1985 *Bulletin of the JSME* **28**, 1240–1246. On the static running accuracy of ball bearings.
15. G. T. FLOWERS and FANG SHENG WU 1993 *Journal of Engineering for Gas Turbine* **115**, 279–286. A study of the influence of bearing clearance on lateral coupled shaft/disk rotordynamics.
16. A. MUSZYNSKA 1996 *Journal of Sound and Vibration* **192**, 207–222. Forward and backward precession of a vertical anisotropically supported rotor.

APPENDIX A: NOMENCLATURE

ω_{cage}	rotational speed of bearing cage, rad/s
ω_{ROTOR}	rotational speed of rotor, rad/s
ω_{vc}	varying compliance frequency, rad/s
γ_0	radial internal clearance, μm
θ_i	angular position of the ith ball in the ball bearing
ε	very small number
R_i	radius of inner bearing race
R_o	radius of outer bearing race
N_b	number of bearing balls
BN	bearing number, $R_i(R_i + R_o)N_b$
C_b	stiffness constant, N/m$^{1\cdot5}$
C	damping, N s/m
K	stiffness, N/m
F_{θ_i}	spring force at the ball at angular location θ_i
F_x	x-component of the resultant spring force
F_y	y-component of the resultant spring force
F_u	unbalance force
T_{VC}	time period of varying compliance vibrations
$T_{Rotational}$	time period of shaft rotation
W	constant vertical force, N